



A theoretical investigation of the Ba₂CePtO₆ double perovskite for optoelectronic and thermoelectric applications

Abderrazak Boutramine¹ · Samah Al-Qaisi² · Malak Azmat Ali³ · Tahani A. Alrebdī⁴ · Afaf Khadr Alqorashi⁵ · Ajay Singh Verma⁶ · Zeesham Abbas⁷ · El Sayed Yousef^{8,9} · Ramesh Sharma¹⁰ · Muhammad Mushtaq¹¹

Received: 21 July 2023 / Accepted: 13 December 2023 / Published online: 18 January 2024

© The Author(s), under exclusive licence to Springer Science+Business Media, LLC, part of Springer Nature 2024

Abstract

In this work, theoretical investigations were performed for the structural, elastic, optoelectronic, thermodynamic, and thermoelectric characteristics of barium ceroplatinate Ba₂CePtO₆ double perovskite oxide. The direct band gaps 1.518 eV and 1.385 are calculated with TB-mBJ potential, and PBE-GGA approximation. The findings of elastic constants C₁₁, C₁₂ and C₄₄, ensure the mechanical stability, ductile nature, anisotropic, Debye temperature, and ionic bonding. In visible and ultraviolet spectrums, Ba₂CePtO₆ exhibits a high absorption coefficient (> 10⁵ cm⁻¹), low optical reflectivity, low electron energy loss and excellent refractive index. Finally, the thermoelectric properties are computed using BoltzTraP code. At room temperature the figure of merit has been reported as 0.84 and 0.998. Therefore, the reported results are likely to serve as an inspiration for the forthcoming experimental and theoretical investigations.

Keywords Double perovskites oxides · Elastic constants · Structural properties · Thermoelectric properties · Optoelectronic properties

1 Introduction

Recently, with the rapid development of humans and the improvement of living standards, the question of energy supply, and many critical ecological issues, have become progressively concerned. In this view, we are dealing with the inevitably depletion of conventional energy resources with adverse effects on the environment (Mostafaeipour et al. 2022; Ivanovski et al. 2021; Snaith 2013). Therefore, seeking out new sustainable energy resources, efficient and economically viable, and especially coping with global warming, are the most pressing current issues (Mantziaris et al. 2017; Bildirici and Gökmenoğlu 2017). In this regard, it is worth mentioning that about 50% of the energy generated from primary sources is discarded as squander heat energy. The use of photovoltaic (PV) and thermoelectric (TE) technologies offers the extremely reliable alternative methods to convert the heat generated from solar radiation and to harvest effectively the industrial waste

heat and automotive exhausts for electricity production. Therefore, the primary challenging task in this research area is to substantially enhance the PV and TE conversion efficiencies as compared to the conventional techniques. This can be attained with the help of fundamental and promising materials for devices origin. The most intrinsic transport parameter used to estimate the TE conversion efficiency of a material is the dimensionless figure of merit, $ZT = S^2\sigma T/\kappa$. In this quantity S , σ , κ , T stand respectively to Seebeck coefficient, electrical conductivity, total thermal conductivity and the absolute working temperature. Therefore, a typical TE material possesses an excellent σ to reduce Joule heating effect, strong S for a maximum heat-to-electricity conversion, and low κ keep a heat at the junctions and retain a substantial temperature gradient. Clearly, the task is to propose a potential material with specific properties that satisfy the basic requirements of optoelectronic and TE technologies.

In recent past, perovskite materials have attracted immense excitement and have been recognized as the material of choice for optoelectronics and TE applications due to their remarkable features (Wu et al. 2015; Soukiassian et al. 2008; Chen et al. 2010). There are many kinds of materials have been studied for optoelectronic and photovoltaic applications (Tarbi et al. 2022, 2023a; b, c). Interestingly, perovskite materials can display many intriguing structural and electro-optical properties which show their flexibility to accommodate many elements of the periodic table. The general stoichiometric formula of simple perovskites structures is ABX_3 , where A denotes a rare earth, alkaline earth or transition metal cation, B is the transition metal cation and X stands to an anion. In the current situation, considering the ABO_3 primitive perovskites oxides, when the octahedral coordinated B cation is shared, with 1:1 proportion, by two distinct transitions metals cations B' and B'' , the $A_2B'B''O_6$ double perovskite oxide (DPO) is formed. A significant difference between the size of B' and B'' transition metal cations play an important role in stabilizing the ordering phenomenon (Lufaso et al. 2006; Anderson et al. 1993). Moreover, the charge balance is maintained by: $2Q_A + Q_{B'} + Q_{B''} = 12$. In the crystallographic point of view, the crystal symmetry and space group of DPOs depend mainly on the arrangement of both $B'O_6$ and $B''O_6$ octahedral (Chen et al. 2005; Retuerto et al. 2004). Furthermore, the potential applications of DPOs as merited a great deal of consideration in many fundamental and applied areas (Tariq et al. 2020; Slavney et al. 2016; Faizan et al. 2016; Rammeh 2016; Bharti and Sinha 2011a) due to their versatile properties such as tunneling magneto-resistance, magneto-optic properties, ferromagnetism, metallicity, multi-ferocity magneto-dielectric properties, high dielectric constants and photo-catalytic activity and so on (Saha-Dasgupta 2020; Yin et al. 2019; Ray et al. 2017; Vasala and Karppinen 2015; Retuerto et al. 2006; Bairwa et al. 2023; Al-Qaisi et al. 2023; Mebed et al. 2023; Das et al. 2008; Kato et al. 2002).

As far as Ba-based DPOs are concerned, an extensive amount of work has already been published (Al-Qaisi et al. 2022a, b; Himanshu et al. 2022; Kockelmann et al. 2006; Korchagina and Shevchuk 2006; Fu and Ijdo 2005; Kazim et al. 2022; Reddy et al. 2018; Aczel et al. 2019; Dutta et al. 2016; Bharti and Sinha 2011b,c; Hatakeyama et al. 2010; Amador et al. 1992). In this regards, Al-Qaisi et al. (2022a) predicted that Ba_2YBiO_6 is an indirect p-type semiconductor (SC) with a high ZT which is suitable for the ultraviolet (UV) and visible (VIS) optoelectronic devices, and TE applications. The same group demonstrates that Ba_2NaIO_6 is a direct p-type SC. Their findings reveal that this compound is a good material for infrared optoelectronic and TE applications (Al-Qaisi et al. 2022b). Based on the synchrotron X-ray diffraction technique and the reflectance measurements in the UV–VIS range, Himanshu et al. (2022) report that Ba_2ScTaO_6 refined in an ordered cubic symmetry with a band gap of 4.7 eV. From the High-resolution neutron powder diffraction

measurements, Kockelmann et al. show that at ambient temperatures Ba₂PrIrO₆ DOP is cubic space group Fm-3m. Also, they demonstrate that below 71 K the compound orders anti-ferromagnetically (Kockelmann et al. 2006). In the experimental work of Korchagina et al., the low-frequency dielectric and microwave features of Ba₂LnTaO₆ (Ln=La, Pr, Sm, Dy, Ce, Gd, Nd, Tm, Tb) compounds were evaluated. The reported results were conveniently correlated with the ionic radius of Ln cations (Korchagina and Shevchuk 2006). In addition, based on X-ray powder diffraction measurements at room temperature, the crystal symmetry of a series of Ba₂LnSbO₆ (Ln=La, Pr, Nd, Sm) DOPs have been explored by Fu and Ijdo. They demonstrate that the structure of Ba₂LnSbO₆ (Ln=La, Pr and Nd) are rhombohedral with the space group \bar{R} not monoclinic or cubic as were previously reported (Fu and Ijdo 2005).

Moreover, after a comprehensive literature review, we have noticed a few works on Ce- containing DOPs. In this respect, using the FP-LAPW method within DFT theory, Kazim et al. ensure that Ba₂CeZrO₆ is stable in cubic symmetry with band gap energy of 3.25 eV. The ZT of 0.65 was observed at 800 K. Therefore, the reported results demonstrated that this compound fits well the optoelectronic and TE applications (Kazim et al. 2022). Furthermore, in their work, Reddy et al. (2018) have prepared Ba₂CeZrO₆ DOPs for the first time using the sol-gel technique. Their results show that the sample is refined in cubic structure with space group Fm-3m with a semiconducting nature. Also, based on neutron powder diffraction results, Aczel et al. (2019) show that Ba₂CeIrO₆ crystallizes in the cubic space group Fm-3m. The structural and magnetic properties of Ba₂CeSbO₆ DPO have been synthesized by Dutta et al. Their Rietveld refinement results suggest the monoclinic ordered structure with an anti-ferromagnetic behavior. The XPS study reveals the existence of two oxidation states of Ce (Dutta et al. 2016). The barium cerium tantalate Ba₂CeTaO₆ has been synthesized and characterized by Bharti and Sinha. Based on XRD patterns, they show that at room temperature the sample crystallizes in a monoclinic symmetry. The frequency-dependent conductivity spectra show that at f=110 Hz the conductivity varies from 3.5×10^{-7} to 1.2×10^{-2} S.m⁻¹ when the temperature increases from 303 to 673 K (Bharti and Sinha 2011b). Furthermore, Ba₂CeNbO₆ DPO was prepared and characterized for the first time by Bharti et al. The XRD data at ambient conditions confirms the monoclinic crystal structure (Bharti and Sinha 2011c). Finally, a series of Ba₂RBiO₆ (R=La, Ce, Nd, Sm, Eu, Gd, Dy) DOPs have been synthesized by Hatakeyama et al. (2010) The high observed photocatalytic activities under VIS irradiation have been interpreted within a first-principle calculation within FLAPW method. Meanwhile, the lack of Pt-containing DOP is observed. On the basis of refinement of the XR powder diffraction pattern, Amador et al. (1992) demonstrate that Ba₂PrPtO₆ is a cubic crystal with Fm-3m space group.

In the current work, we are focusing on barium ceroplatinate Ba₂CePtO₆ DPO for the motivated following reasons: To the best of our knowledge, except the below mentioned works, there are no reports on the properties of Ba₂CePtO₆ encountered in the literature. Furthermore, due to its nontoxic aspect it can be a potential material for useful applications. Additionally, owing to its reasonable direct semiconducting band gap, it can be selected as a plausible candidate for optoelectronic and TE and PV conversions. The formation of Ba₂CePtO₆ was first observed by Ouchetto et al. (1991), while working on the synthesis of barium procreates perovskite type (BaCeO₃) in the platinum (Pt) crucibles in air using hydrothermal method. Accordingly, Ba₂CePtO₆ comes from the reaction between the synthesized BaCeO₃ and Pt and air/O₂. The structure determination was performed from the intensities of 15 diffraction peaks, up to $d_{hkl}=0.1$ nm, while, the space group was deduced from the systematic existence condition (hkl): $h+k, k+l, h+l=2n$. As a result,

Ouchetto et al. (1991) conveniently concluded that their DOP crystallizes in a cubic $Fm\bar{3}m$ space group ($n=0.225$) with a primitive cell parameter $a=8.4088 \text{ \AA}$. Furthermore, in the primitive unit cell the Wyckoff positions of Ba, Ce, Pt and O atoms are, respectively, 8c, 4b, 4a and 24e with coordinates $(1/4, 1/4, 1/4)$, $(1/2, 1/2, 1/2)$, $(0, 0, 0)$ and $(0.248, 0, 0)$ as displayed in Fig. 1. Moreover, Casapu et al. (2007) discovered Ba_2CePtO_6 DPO while dealing with a Pt/Ba/CeO₂ catalyst and suggested a reaction in which a BaPtO₃ compound is first formed and reacts with BaCeO₃ to form the Ba_2CePtO_6 DPO.

In this light, the primary purpose of the current study is to show to what extent this newly predicted material can be used for optoelectronics devices and PV and TE conversion purposes. For this aim, we have convincingly investigated the structural, elastic, optoelectronic, and TE properties of this proposed material. The rest of the present manuscript is structured as follows: in Sect. 2, the computational method details are described. The results and discussions are presented in Sect. 3 where a comparison is made, when possible, with similar compounds. Finally, in the last section we conclude this work with a summary of the reported results.

2 Computational method

To simulate the crystal primitive cell of Ba_2CePtO_6 we have adopted the previously mentioned experimental structural parameters measured by Ouchetto et al. (1991). Subsequently, the structural, elastic, optoelectronic, thermodynamic and TE properties were performed within the frame of density functional theory (DFT) using the full-potential linearized augmented plane wave plus local orbital (FP-LAPW+lo) method as implemented in the WIEN2K software package (Schwarz et al. 2002; Madsen et al. 2001; Blaha et al. 2001). In this method, a muffin-tin crystal potential is presupposed and the crystal primitive unit cell is partitioned into two regions: (i) non-overlapping muffin-tin spheres (MTS) with radii R_{MT} centered at the atomic sites and separated by (ii) an interstitial space. In addition, these two regions were properly treated with different basis sets. Inside the non-overlapping MTS, the electron is

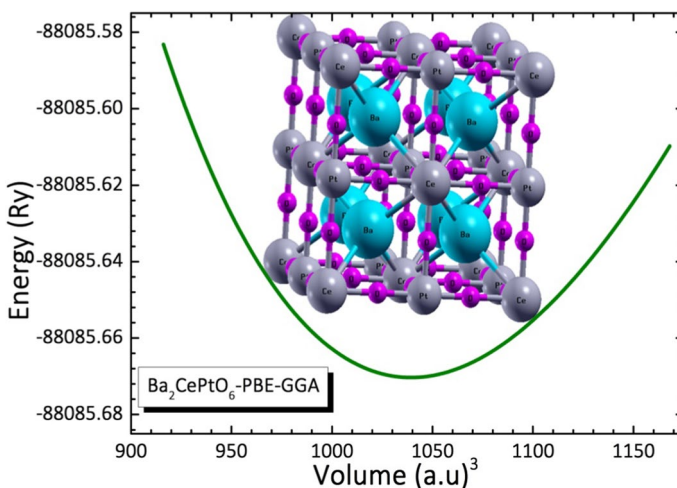


Fig. 1 The crystal structure and the calculated total energy as a function of volume $E(V)$ for the cubic Ba_2CePtO_6 optimized structure using PBE-GGA

extended in terms of radial functions times spherical harmonic basis functions in the interstitial and plane wave regions. Within the MT spheres, the basis set is adequately controlled with the maximum angular momentum $l_{\max} = 10$. While in the interstitial space, a reasonable number of plane wave functions for $K_{\max}(\text{a.u.})^{-1} = 7/(R_{\text{MT}})_{\min}$ is adopted, where K_{\max} denotes the highest k-vector magnitude, while $(R_{\text{MT}})_{\min}$ is the lowest value amongst RMTs. In the present contribution, RMTs of 2.5, 2.17, 2.04, and 1.67 are chosen for the Ba, Ce, Pt, and O atoms, respectively. These values are adjusted in a fashion that no leakage of electrons occurs from the core into interstitial region and thus the convergence of the total energy is achieved with a minimal time calculation.

After simulating the crystal primitive unit cell, elastic and structural properties of the present material were optimized using the exchange–correlation functional to evaluate by generalized gradient approximation (GGA) in the scheme of Perdew–Burke–Ernzerhof (PBE) functional (Perdew et al. 1996). Subsequently, the computed ground states energies were added into the Birch–Murnaghan equation of state (EOS) to extract the lattice parameter (Murnaghan 1944). Similarly, for the electronic band structure computation, we have executed both PBE–GGA and Trans–Bhala modified Becke–Johnson (TB–mBJ) exchange–correlation potentials (Tran and Blaha 2009). Therefore, to overcome the failing of PBE–GGA to maintain reliable band gap, the outcomes of TB–mBJ approach were appropriately used in the computation of the optoelectronic properties for an incident photon energy range of 0–14 eV. As accessible in the WIEN2K software package (Schwarz et al. 2002; Madsen et al. 2001; Blaha et al. 2001), a dipole matrix element approach was adopted to conduct the optical features, with a Lorentzian broadening parameter of 0.1 eV. Additionally, the TE transport properties were investigated in the framework of the Boltzmann semi-classical transport theory under the constant relaxation time (τ) and rigid-band approximations. Subsequently, the TE transport equations were implanted in the BoltzTrap code with $\tau = 10^{-14}$ s (Madsen and Singh 2006). Moreover, the Integrations over the FBZ were performed using non-shifted k-points mesh of 3000 ($14 \times 14 \times 14$) for optoelectronic and 124,000 ($49 \times 49 \times 49$) for TE transport properties because they require dense k-mesh. Moreover, a self-consistency is reached when the system total energy convergence between two successive iterations is lower than 10^{-5} Ry.

3 Results and discussion

3.1 Structural properties

At the first stage and before starting the detailed computation, it is necessary to determine the most stable structure of Ba₂CePtO₆ in its ground state. For this purpose, an accurate optimization of the structural parameters of the interest compound and the relaxed atomic positions were initially conducted within the frame of PBE–GGA approximation by minimizing the system total energy against the primitive unit cell volume $E_{\text{tot}}(V)$. Therefore, the ground state properties of Ba₂CePtO₆ compound, namely equilibrium lattice parameter a_0 , equilibrium primitive unit cell volume V_0 , bulk modulus B_0 and its first derivative B_0' have been obtained through the fitting of $E_{\text{tot}}(V)$ to the Birch–Murnaghan EOS (Murnaghan 1944):

$$E_{\text{tot}}(V) = \frac{VB_0}{B_0'(B_0' - 1)} \left(\left(\frac{V_0}{V} \right) + B_0' \left(1 - \frac{V}{V_0} \right) - 1 \right) + E_0 \quad (1)$$

On the $E_{\text{tot}}(\text{V})$ optimization curve depicted in Fig. 1, the minimum point gives the ground state total energy. Since the perfectly cubic perovskite structure is concerned, the lattice parameter corresponding to the minimum energy is determined at the optimized volume. The obtained results are shown in Table 1. Interestingly, the optimized lattice parameter a_0 reported in this work matches with the experimental value reported in Ouchetto et al. (1991). However, owing to the deficiency in the theoretical and experimental results regarding B_0 and B_0' , for the present compound, our results are predictions.

Furthermore, in this optimized structure the Ba–Ce, Pt–O, Ce–O and Ba–O chemical bond lengths were found to be 3.684, 2.038, 2.216 and 3.009 Å, respectively. These obtained values can directly employ to give the first idea on the nature of chemical bonds in $\text{Ba}_2\text{CePtO}_6$. Therefore, the distance Pt–Ce is about 4.254 Å, which is in the same order as $a/2$ parameter. Besides, the shortest distance between Ba and Ce is less than the sum of the two atomic radii. Furthermore, the distances between O atom and other atoms are lower than the sum of the corresponding atomic radii. All these indications ensure its strong bonding and preservation. Another remark that should be pointed out is that the stability of the material under focus depends mainly on the mutual suitability of Ba^{2+} , Ce^{3+} , Pt^{5+} , and O^{2-} ions in terms of their atomic radii characterized by the tolerance factor τ defined as follows (Bharti and Sinha 2010):

$$\tau = \frac{r_{\text{Ba}} + r_{\text{O}}}{\sqrt{2} \left(\frac{r_{\text{Ce}} + r_{\text{Pt}}}{2} + r_{\text{O}} \right)} \quad (2)$$

The perfectly cubic perovskite material is usually predictable when $\tau = 1$. In the current work, the tolerance factor of 1 was obtained confirming that $\text{Ba}_2\text{CePtO}_6$ compound stabilizes in a perfect cubic perovskite structure. The accuracy of our results implies the reliability of to the current work and inspired us to investigate different properties of the $\text{Ba}_2\text{CePtO}_6$ DOP.

Table 1 The computed structural parameters of the optimized crystal structure and band gap of $\text{Ba}_2\text{CePtO}_6$ DOP

Parameters		Present	Experimental (Ouchetto et al. 1991)
Lattice constant (Å)		8.5089	8.4088
Bulk modulus (GPa)		147.31	–
First derivative of bulk modulus (GPa)		4.55	–
Ground-state total energy (Ry)		–88,085.67	–
Bond lengths (Å)	Ba–Ce	3.684	–
	Pt–O	2.038	–
	Ce–O	2.216	–
	Ba–O	3.009	–
Tolerance factor		1.00	–
Band gap energy (eV)	PBE-GGA	1.385	–
	TB-mBJ	1.518	–

3.2 Elastic properties

To inspect the mechanical behavior of a material for specific application, mechanical properties play a primordial role because they are linked to different micro and macroscopic properties of materials. These mainly include the elastic constants (C_{ij}), Shear (G), Bulk (B), and Young (Y) moduli. They allowed us to examine the possible features of a material in terms of its mechanical stability, brittleness, ductility, anisotropy, nature of the inter-atomic bonding, melting temperature, sound velocity, and Debye temperature and so on. Furthermore, in the present contribution, as the perfect cubic symmetry is concerned, the axial lengths are equal; therefore, only three independent elastic constants in the C_{ij} tensor are required namely C_{11} , C_{12} and C_{44} . Our results yield values of $C_{11}=283.97$, $C_{12}=78.98$ and $C_{44}=59.3$ GPa as listed on Table 2. It is obvious that the suggested compound is characterized by a large value of C_{11} contrasted to C_{12} and C_{44} , implying that Ba₂CePtO₆ has more withstanding resistance to unidirectional compressive strength than shearing deformation. The elastic stability of the present material requires that the whole set of C_{ij} must fulfill the Born elastic stability criterion: $C_{11}, C_{12}, C_{44} > 0$; $C_{12} < B < C_{11}$; $C_{11} - C_{12} > 0$ and $C_{11} + 2C_{12} > 0$ (Wang et al. 1993; Behera et al. 2023).

The evaluated C_{ij} for Ba₂CePtO₆ are positive in the unit of GPa and adequately content with the mentioned stability conditions, implying that the current compound is mechanically stable. Thus, this result accurately allowed us to conduct the present investigation. A part from that, it is not useful to study a material that is not mechanically stable. Subsequently, the obtained C_{ij} can be used to determine the macroscopic behavior of the material under focus. Hence, for industrial point of view applications, the key elastic coefficients namely shear (G), bulk (B), Young (Y) moduli, Cauchy pressure (CP), Pugh index (B/G), Poisson ratio (ν), anisotropic factor (A) are computed and listed in Table 2.

The G elastic modulus provides indications on the plastic deformation of a compound through an external pressure. G is the arithmetic average of G_V and G_R which represent its upper and lower limiting values, respectively, obtained from $G = (G_R + G_V)/2$ where $G_V = (C_{11} - C_{12} + 3C_{44})/5$ and $G_R = 5(C_{11} - C_{12})C_{44}/(3(C_{11} - C_{12}) + 4C_{44})$ (Hill 1952). Therefore, by referring to Table 2, the recorded value of $G = 73.95$ GPa suggests that Ba₂CePtO₆ shows greater resistance plastic deformation compared to Ba₂ZrCeO₆ (Kazim et al. 2022). Also, the bulk modulus $B = (C_{11} + 2C_{12})/3$ (Hill 1952) is a proper quantity used to

Table 2 Computed elastic and thermodynamic parameters of Ba₂CePtO₆

Parameters		Ba ₂ CePtO ₆	Ba ₂ ZrCeO ₆ (Kazim et al. 2022)
Elastic constant (GPa)	C_{11}	283.97	–
	C_{12}	78.98	–
	C_{44}	59.30	–
Cauchy pressure C_p (GPa)		19.68	–
Bulk modulus B(GPa)		147.31	138.51
Shear modulus G(GPa)		73.95	–
Young modulus Y(GPa)		190.05	–
Pugh ratio B/G		1.99	–
Poisson ratio ν		0.284	–
Anisotropic factor A		0.58	–

determine the resistance towards the volume change in response to external pressure. As a result, B (GPa) = 147.31 (~2G) indicates that Ba_2CePtO_6 is resistant to the volume deformations than to the shear stress. Furthermore, the Y modulus can be defined as the ratio of linear stress to strain. Also, Y is a proper quantity used to predict the stiffness of a material. Further, the Y modulus is directly evaluated in terms of the computed values of bulk B and shear G moduli using $Y = 9BG/(3B + G)$ (Wang et al. 1993). In this contribution, the predicted value of $Y = 190.05$ GPa advocates that Ba_2CePtO_6 is relatively stiffer compared to Ba_2CeNbO_6 (Bharti and Sinha 2011c). This result is expected to be ascribed to the strong bond between adjacent atoms. Additionally, the reported moduli decrease in order of $G < B < Y$, implying that this compound reveals more shape deformation than volume deformation.

Also, B and G afford important indication regarding the malleability of materials through Pugh index (B/G) (Pugh 1954). In this context, the amount value of the Pugh index is typically 1.75 for purely plastic materials. If B/G is smaller than 1.75, a brittle attitude is predicted, else the material is designated as ductile (Bougherara et al. 2022). Besides, for the compound of interest, the value of B recorded in Table 2 is two times larger than G suggesting the ductile behavior of Ba_2CePtO_6 . This result is supported by the Cauchy pressure ($C_p = C_{12} - C_{44}$) (Pettifor 1992). C_p manifests as an effective way to identify the brittle and ductile behavior of a material in such a way that if $C_p > 0$ the material is ductile. Otherwise, as for a brittle structure $C_p < 0$. Further, the positive C_p observed for the Ba_2CePtO_6 DOP ensures that this material shows a ductile behavior. In the same way, the ductility nature of the present material can be confirmed using the Poisson ratio. The Poisson ratio, $\nu = (3B - Y)/6B$, represents the volumetric change throughout uniaxial deformation (Li et al. 2012). Thus, for a completely plastic compound, a critical amount of ν is close to 0.26. However, if $\nu < 0.26$, the compound shows a brittle nature, while, if $\nu > 0.26$, the material affords ductile character. Based on these conditions, the present reported value of ν is about 0.285. Thus, the ductility of Ba_2CePtO_6 compound is accounted again. Accordingly, Ba_2CePtO_6 is an excellent candidate for device fabrication. Also, the good approval emphasizes the reliability and precision of the current study. In other hand, the chemical bonding character in a material can be outlined from the above mentioned ν . For covalent materials, $\nu \sim 0.1$, whereas a material exhibits an ionic bonding if $\nu = 0.25$. However, as for a metallic material $\nu = 0.33$ (Rani et al. 2023). Accordingly, as reported in Table 2, the stability of the suggested material is maintained by ionic bonding with metallicity and hence showing ductile nature. In addition, the direction-dependent elastic properties of a material can be identified using the anisotropic factor $A = 2C_{44}/(C_{11} - C_{12})$ evaluated from the elastic constants (Li et al. 2012). As a matter of fact, the elastic anisotropy originates basically from the difference in the longitudinal and shear elastic constants. For a purely isotropic material $A = 1$, otherwise the divergence from unity indicates the degree of elastic anisotropy. For the Ba_2CePtO_6 DOP, the recorded $A = 0.58$ inferred that the investigated compound present anisotropic character and can therefore exhibits different properties in various directions.

3.3 Thermodynamic properties

Likewise, another indispensable physical parameter, known as melting temperature (T_m), has been estimated under ambient conditions. The T_m is the critical temperature of a solid above which it starts melting and changes phase from solid to liquid. The value

of T_m of a crystal is linked to the directional elastic constant C_{11} and can be predicted through the standard equation (Dar et al. 2019):

$$T_m = \left(553 + \left(\frac{5.91}{GPa} \right) C_{11} \right) \pm 300 \text{ (K)} \tag{3}$$

The present reported value of $T_m = 2231 \pm 300$ K is consistent with what we concluded for Y modulus. Also, it confirms the strong bonding and retention of the studied material and provides a strong validation for its practical use for elevated temperatures applications. Furthermore, the average sound velocity v_m , also known as average Debye velocity, is expressed in terms of transverse and longitudinal parts velocities as (Jasiukiewicz and Karpus 2003):

$$v_m = \left(\frac{1}{3} \left(\frac{2}{v_t^3} + \frac{1}{v_l^3} \right) \right)^{-\frac{1}{3}} \tag{4}$$

where v_t and v_l are the magnitudes of transverse and longitudinal sound velocities, respectively. By means of the computed value of, B and G, the v_t and v_l can be estimated through Navier equation of states $v_t = (G/\rho)^{0.5}$ and $v_l = (3B + 4G/3\rho)^{0.5}$ (Schreiber et al. 1975). Evidently, the sound velocities depend on the B and G, indicating that higher values of elastic moduli imply high values of sound velocities as well. Our results concerning v_t , v_l and v_m for Ba₂CePtO₆ are given in Table 3. Thus, one can note that the v_l is about 1.82 higher than v_t . The Debye temperature (T_D) is a material basic quantity directly linked to various physical properties namely lattice vibrations, thermal conductivity and so on. Moreover, the T_D directly affects the specific heat capacity of a solid. Interestingly, T_D is predicted from the computed C_{ij} elastic constants through the average sound velocity v_m mentioned above by the following expression (Jasiukiewicz and Karpus 2003):

$$T_D = \frac{h}{k_B} \left(\frac{3n N_A \rho}{4\pi M} \right)^{\frac{1}{3}} \times v_m \tag{5}$$

where h is Planck’s constants, k_B is Boltzmann’s constant, n stands to the number of atoms per unit cell, N_A is Avogadro’s number, ρ is for the density, M represents the molecular mass per unit cell. Thus, Ba₂CePtO₆ has more withstanding to heat generated by lattice vibration. Also, this alloy can be considered as a low thermal conduction material which could be interesting for TE applications. The obtained values are recorded in Table 3. Due to the unavailability of both theoretical and experimental data of T_m , v_m and T_D of

Table 3 The computed thermodynamic parameters of Ba₂CePtO₆ DOP

Parameters	Ba ₂ CePtO ₆
ρ (g/cm ³)	7.61
Melting temperature T_m (K)	2231 ± 300
Transverse sound velocity v_t (m/s)	3117.19
Longitudinal sound velocity v_l (m/s)	5684.42
Average sound velocity v_m (m/s)	3475.29
Deby temperature T_D (K)	415.86

the current material, a comparison has been made with the data related to similar DOPs compounds.

3.4 Electronic properties

After checking the structural stability and formability of $\text{Ba}_2\text{CePtO}_6$ DPO, it is of crucial importance to conduct their substantial optoelectronic performances through an in-depth insight into its electronic band structure and the related total (TDOS) and partial density of states (PDOS). Indeed, knowing the band structure features of a material accurately provides valuable information for their synthesis and manufacturing.

3.4.1 Electronic band structure

The band structure calculated with PBE-GGA and TB-mBJ potentials along with the total density of states are illustrated in Fig. 2a–c. The Fermi level (E_F) taken at zero is selected to be the energy reference. As depicted in Fig. 2a, b, the bands structure patterns obtained with PBE-GGA and TB-mBJ potentials conceptually simulate each other. Accordingly, it can be inferred that the compound under focus shows that the conduction band minimum (CBm) and the valence band maximum (VBM) are revealed at X-point of the FBZ, confirming the existence of a direct (X–X) band-gap (E_g). Furthermore, as regards to the magnitude of E_g , we have recorded the values of 1.385 eV and 1.518 eV within PBE-GGA and TB-mBJ approaches, respectively. However, it should be noted that the gap energy value is underestimated by about 9% within PBE-GGA potential. Therefore, the band gap value has been enhanced using TB-mBJ potential. Consequently, the present E_g agree reasonably with those of stable and direct compounds appropriate for PV conversion (1.35–2.4) eV.

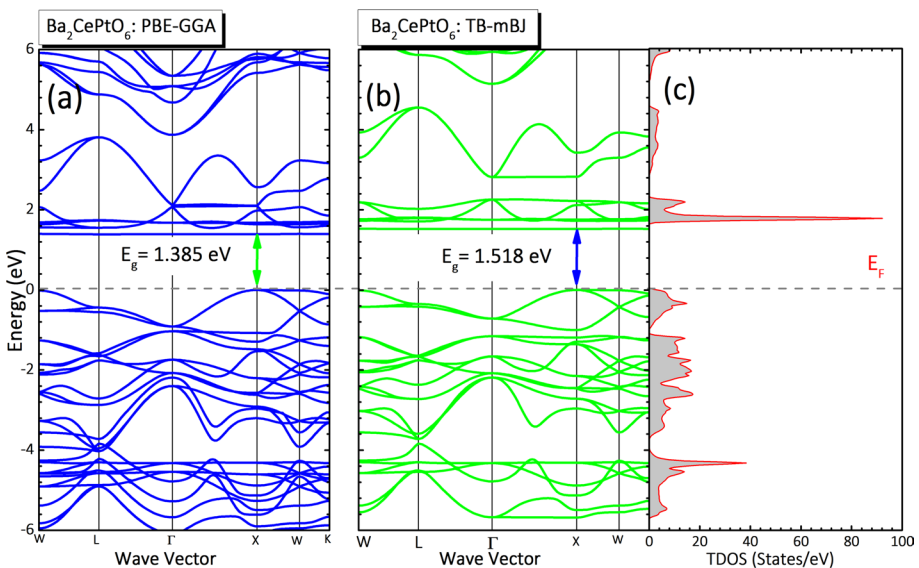


Fig. 2 The computed electronic band structure for $\text{Ba}_2\text{CePtO}_6$ using **a** PBE-GGA and **b** TB-mBJ approaches. **c** represents the corresponding total density of states (TDOS)

Moreover, a close examination of Fig. 2a, b shows that the group of CBs is slightly shifted to higher energies in the case of TB-mBJ potential inducing the enhanced $E_g(X)$. However, in all circumstances, the E_F level seems to do not cross the energy bands. Accordingly, the material under focus exhibits a semiconducting behavior.

The proposed DPO material not only exhibits a semiconducting direct E_g but also it shows substantial flatter bands along the (X–W–K) path. This results in an enhancement of the probability of electron transition from VBM states to CBm states associated with a photon absorption. Interestingly, the lowest CB is almost flat in the whole BZ, whereas the highest VB shows a notable dispersion. The observed flatness in the first CBs indicates that the individual electrons are weakly affected by each other. Also, this feature lead to a small hole's effective masse with extremely high mobility allowing a p-type conductivity character. Moreover, the presence of p-type semiconducting nature is shown by the closeness of E_F level to VB. In the absence of both theoretical and experimental findings to be contrasted with our data regarding the magnitude of E_g of Ba₂CePtO₆ DPO, and owing to the fact the present findings are obtained from the TB-mBJ framework, we expect that the present results are more accurate. Also, since the present compound is characterized by moderate and direct band gap, it can be believed as a potential candidate for PV and TE conversion applications.

3.4.2 Density of states

As means to provide sufficient explanation about the electronic properties and to inspect the provenance of electronic states in the computed band structure, the partial (PDOS) and total (TDOS) density of states as a function of energy were computed in the TB-mBJ potential framework. The obtained results, projected between –6 and 6 eV, are shown in Fig. 3a–c. Clearly, one can observe that diverse peaks with high TDOS dominate both valence and conduction regions suggesting the availability of a large number of unoccupied electronic states. A close inspection of these figures reveals that in the energy range of –6 to –4 eV of the lowest VBs, the TDOS is typically originates from the Pt-5d, O-2p and Ba-p bonding orbitals, where the predominant contribution of the Pt-5d is larger than that of O-2p and Ba-p. Furthermore, in the energy range extending from –4 to –1 eV, the significant contributions are provided by the O-2p orbital and the p and f-type orbitals of Ce atom. Moreover, the CB as a whole is mainly constituted by the unoccupied Ce-4f, Pt-5d, and p-type states of O and Ce atoms. Therefore, one may say that the main contributions are due to the Ce-4f and Pt-5d with a little involvement from the O-2p and Ce-2p orbitals. A further consideration of these results specifies that the edge associated with the VBM has a contribution from Pt and O atoms, while CBm is mainly obtained from Ce atom with a slight contribution from Pt and O atoms. Besides, the band gap energy is characterized by direct transitions from the dominating Pt-5d metal states in VB to the dominating Ce-4f states in CB.

It is a known fact that the optoelectronic features of SC compounds are tightly related to the distribution of states around the E_F level. For the DPO under focus, these results highlight that for the upper VBs near the E_F level, the most important contribution originates basically from the 5d electrons of Pt atom with a few contributions of O-2p states. This indicates that the Pt-5d electrons have an interesting role in the conductivity of the present material. Besides, in the valence region, a small value of TDOS at the E_F level explains the p-type semiconducting nature for this material. While in CB regions the TDOS vanishes

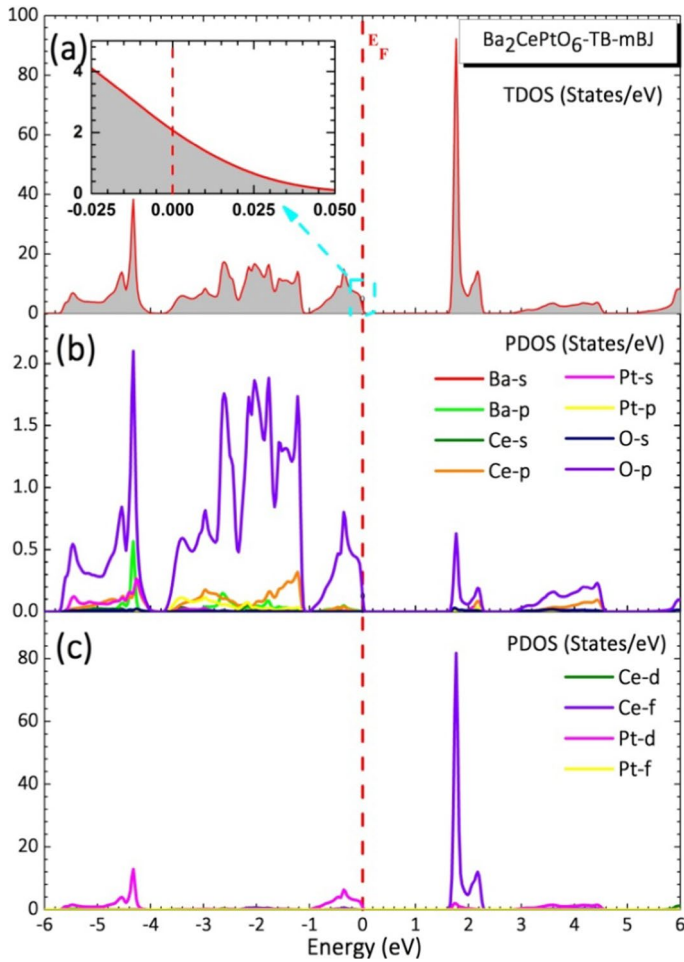


Fig. 3 The partial (PDOS) and total (TDOS) density of states for $\text{Ba}_2\text{CePtO}_6$ computed within the frame of TB-mBJ approximation

at the E_F level. Furthermore, the value gap of 1.52 eV closes to the E_F level in TDOS confirms the SC character of our material.

3.5 Optical properties

The optical characteristics exhibit the light transmission, transparency and polarization ability of materials in different energy ranges, which can be regarded as important indexes for the study of optoelectronic materials. Actually, the key function which can precisely describe the optical behavior of a material owing to an external electromagnetic (EM) radiation is the frequency-dependent complex dielectric function $\epsilon(\omega)$. From the theoretical point of view, $\epsilon(\omega)$ can be split into two parts as given by Ehrenreich and Cohen as $\epsilon(\omega) = \epsilon_1(\omega) + i\epsilon_2(\omega)$ (Hilal et al. 2016), where $\epsilon_1(\omega)$ and $\epsilon_2(\omega)$ stand to the real and the

imaginary components of $\epsilon(\omega)$, correspondingly. Mostly, ϵ is a tensor with nine different direction-depending components. However, with regard to the crystallographic symmetry, only some of these components may be independent. As Ba₂CePtO₆ compound crystallizes in cubic phase, the three principal x, y, and z directions are equivalent. Accordingly, the principal tensor components are equal: $\epsilon_{xx} = \epsilon_{yy} = \epsilon_{zz}$. Therefore, it is crucial to compute only one component. The imaginary component $\epsilon_2(\omega)$ of the dielectric function can be achieved by summing up, over the first Brillouin zone (FBZ), all possible transitions of the electrons from the occupied electronic states at the VB to the empty states at the CB. Considering the appropriate transition dipole matrix elements, $\epsilon_2(\omega)$ can be stated in the following form (Al-Qaisi et al. 2021):

$$\epsilon_2(\omega) = \left(\frac{2\pi e}{m\omega}\right)^2 \sum_{ij} \int_{BZ} \langle i|M|j\rangle \times f_i(1 - f_j) \times \delta(E_{j,k} - E_{i,k} - \omega)d^3k \tag{6}$$

where e stands to the elementary charge, m is the electron mass, M denotes the dipole matrix element, $\langle i|$ and $|j\rangle$ represent the initial and final electronic states, respectively, $E_{i,k}$ presents the energy level of the electron in the i th state, f_i stands to the Fermi distribution function taken for the i th state. Indeed, $\epsilon_1(\omega)$ and $\epsilon_2(\omega)$ are interlinked by the Kramers–Kronig relation (Bobrov et al. 2010):

$$\epsilon_1(\omega) = 1 + \frac{2P}{\pi} \times \int_0^\infty \frac{\omega' \epsilon_2(\omega')}{\omega'^2 - \omega^2} d\omega' \tag{7}$$

where P represents the principal value of the Cauchy integral.

Thereafter, all other optical response functions namely the refractive index $n(\omega)$, the optical absorption coefficient $\alpha(\omega)$, the optical conductivity $\sigma(\omega)$, the extension coefficient $\kappa(\omega)$, the optical reflectivity $R(\omega)$ and the electron energy loss $L(\omega)$ can be derived from $\epsilon_1(\omega)$ and $\epsilon_2(\omega)$ (Gajdoš et al. 2006).

3.5.1 Dielectric function

The dispersion of light energy has been illustrated in Fig. 4a by $\epsilon_1(\omega)$ from which it is obvious that in the low photon energy side, the highest dispersion of light is 7.42 near the energy 1.73 eV corresponding to the resonance frequency in the visible band (VIS). The highest value of $\epsilon_1(\omega)$ spectra in the VIS windows indicates that the materials under load can be efficiently used for PV conversion and for other optoelectronics devices. Afterwards, $\epsilon_1(\omega)$ shows a set of minor peaks essentially attributed to the CB and VB inter-band optical transition. A slight enhancement in the photon energy declines these peaks drastically to their lowest values in the ultraviolet (UV) region. Furthermore, the photons in the energy range from 8.53 to 9.86 eV, and $\epsilon_1(0)$ show that the longitudinal waves are possible. Thereafter, $\epsilon_1(\omega)$ value becomes negative in energy regions from 8.53 to 10.95 eV. Moreover, for the positive values of $\epsilon_1(\omega)$, the photons propagate through the compound under focus, whereas the negative values describe the damping of the incident photons corresponding to the maximum reflection clearly shown by the maximum of reflectivity. The zero energy limit of $\epsilon(\omega)$ or static dielectric constant $\epsilon(\omega \rightarrow 0)$ is the value of $\epsilon(0) = \epsilon_1(0)$ estimated for zero frequency with neglecting the phonon contribution. As depicted on Table 4, the extracted value of $\epsilon_1(0) = 5.11$ for Ba₂CePtO₆ is higher than $\epsilon_1(0) = 4.20$ reported by Kazim et al. (2022) for Ba₂ZrCeO₆ DPO. Moreover, this relatively larger value of $\epsilon(0)$ dictates the

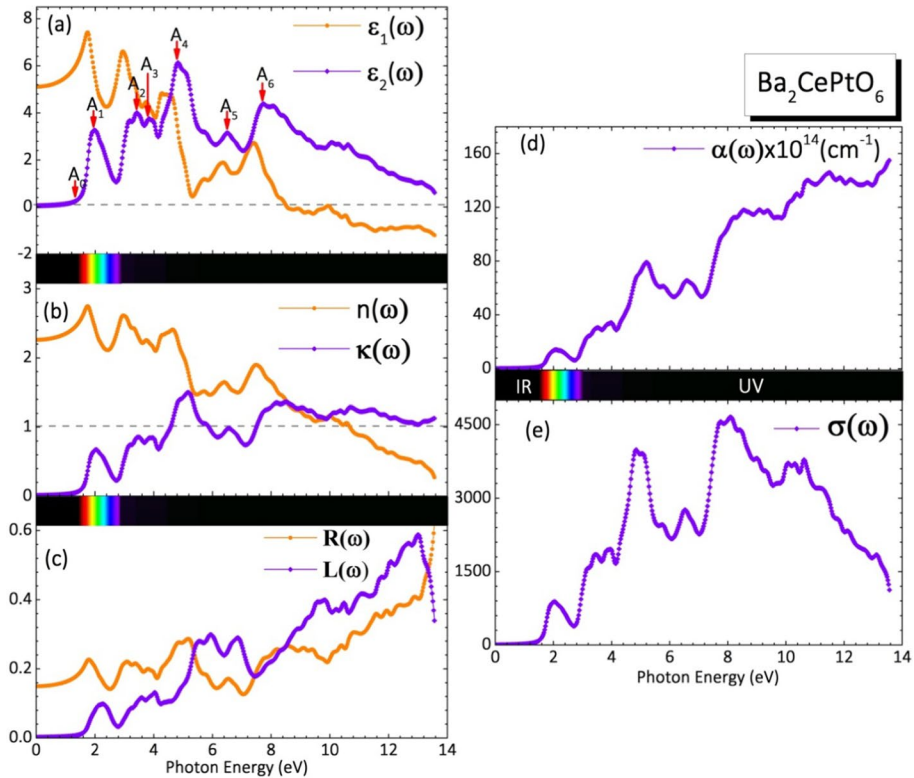


Fig. 4 Computed results of **a** real $\epsilon_1(\omega)$ and imaginary $\epsilon_2(\omega)$ part of the complex dielectric function **b** refraction index and Extinction coefficient **c** electronic energy loss and optical reflectivity **d** absorption coefficient and **e** optical conductivity of Ba₂CePtO₆ compound

Table 4 Computed E_g using PBE-GGA and TB-mJB potentials and cut off values of various optical parameters calculated for Ba₂CePtO₆ DPO along with the reported values for Ba₂ZrCeO₆

Parameters	E_g (eV)		$\epsilon_1(0)$	$n(0)$	$R(0)$
	PBE-GGA	TB-mJB			
Ba ₂ CePtO ₆	1.385	1.518	5.11	2.26	0.15
Ba ₂ ZrCeO ₆ (Kazim et al. 2022)	–	3.25	4.20	2.05	0.12

relatively higher polarizability of Ba₂CePtO₆ material which causes a better optical absorption, and therefore, improves low-level of electronic defects and decreases the radiative recombination. This result is expected owing to the fact that Pt atom has an extra polarization compared to Zr due to its bigger atomic radius. On the other hand, it has also been remarked that the larger $\epsilon_1(0)$ are attributed to the small band gap SCs in consistent with the mathematical equation of the Penn model: $\epsilon_1(0) = 1 + (\hbar\omega_p/E_g)^2$ (Penn 1962).

By referring to the computed $\epsilon_2(\omega)$ spectra depicted in Fig. 4a, one can see that $\epsilon_2(\omega)$ remains zero for an incident photon energy less than that of the first optical critical point

A_0 at which the energy referred to as the fundamental absorption threshold. Thus, the optical E_g can be extracted by the threshold energy of $\epsilon_2(\omega)$ at about 1.52 eV in consistent with the E_g obtained directly from band structure. In Fig. 4a a set of peaks are observed at 1.97, 3.41, 3.85, 4.83, 6.51, 7.74 and 8.07 eV. Moreover, these peaks come chiefly from the most probable direct electronic transferences from occupied electronic states in VBs to the empty states in the CBs. By means of DOS diagram and band structure, it can be realized that A_1 peak is mainly related to transition of the Pt-5d electrons to Ce-4f states. Whereas, the peaks A_2 , A_3 , and A_4 are mainly connected to the optical transitions of electron from 5d orbital under the E_F to the 5d orbital above the E_F of Pt atom. Additionally, the peak A_5 is attributed to the transition of Pt-5d electrons to O-2p states above E_F . These peaks are followed by other minors peaks related to inter-band transitions of electrons between O-2p states below and above E_F .

3.5.2 Refraction index and extinction coefficient

The absorption and optical transparency of materials are basically measured by the extinction coefficient $\kappa(\omega)$ and refractive index $n(\omega)$. In this regard, the $n(\omega)$ index is regarded as the parameter by which the radiation speed and wavelength are reduced compared to their vacuum values. In other words, it describes the transparency degree of a material. In addition, the ionic polarization and local field inside the material is connected to $n(\omega)$ index. Moreover, $\kappa(\omega)$ appears due to the consequence of the propagating EM radiation in the same material medium. Also, the attenuation of EM waves in a material is directly described by the $\kappa(\omega)$ coefficient.

In this work, the computed absorption and transparency of light in terms of $n(\omega)$ and $\kappa(\omega)$ are plotted in Fig. 4b. The trend of these two spectrums is alike to $\epsilon_i(\omega)$. This can be made clearer by looking at the link between these parameters through the relations: $2n\kappa(\omega) = \epsilon_2(\omega)$ and $n^2(\omega) - \kappa^2(\omega) = \epsilon_1(\omega)$. Further, at $\omega \rightarrow 0$ limit, the static $n(\omega \rightarrow 0)$ of the present material is recorded as $n(0) = 2.26$. The spectra of $n(\omega)$ exhibits a set of appreciable peaks principally ascribed to the excitonic transitions. Moreover, these peaks are more intense at low photon energy and this effect is diminished with increasing photon energy. In addition, we can clearly observe that $n(\omega)$ is considerable for a weak incident photon energy. However, it decreases speedily at higher energies in the shape of fluctuations to 14 eV. Its values in the VIS spectrum $n(\omega)$ has peak value 2.75 at 1.76 eV. Thus, the material under focus possesses high $n(\omega)$ within VIS region which is significantly suitable for optoelectronic devices. The situation is extremely quite different for Ba₂ZrCeO₆ which exhibits a pronounced principal peak at around 4 eV situated in UV region (Kazim et al. 2022). Also, the $n(\omega)$ index is less than unity beyond 10.7 eV, implying that Ba₂CePtO₆ material is more refractive. Accordingly, the optical transparency of this material extends over a large range of solar spectrum from UV to IR. Similarly, Fig. 4b displays the $\kappa(\omega)$ coefficient of the Ba₂CePtO₆ DPO. One can note that the $\kappa(\omega)$ values are zero till the fundamental E_g , indicating that the photons will be fully transmitted without any attenuation. Moreover, the $\kappa(\omega)$ coefficient of Ba₂CePtO₆ have many distinct peaks located in both VIS and UV regions, indicating the maximum penetration of light in this region with a strong extinction effect in the UV region. Also, we can see clearly that the peaks $\kappa(\omega)$ are consistent with that of $\epsilon_2(\omega)$. Therefore, one expects that Ba₂CePtO₆ compound is an excellent candidate for optoelectronic applications.

3.5.3 Absorption coefficient

The absorption coefficient $\alpha(\omega)$ characterizes the distance traveled by the incident photons inside a material before absorption. In other word, it deals with the change in the intensity of light at a given wavelength per unit length. With regard to the design and fabrication of optoelectronic and PV devices, $\alpha(\omega)$ is the most compelling and sensitive criteria for checking the ability and usefulness of SC materials. For this purpose, $\alpha(\omega)$ has been computed for $\text{Ba}_2\text{CePtO}_6$ DPO in the incoming photon energy range of 0–14 eV. The obtained spectrum is illustrated in Fig. 4d. The noticed peaks are consistent with that of $\epsilon_2(\omega)$ and $\kappa(\omega)$. Additionally, it is noteworthy that the wider peaks are resulted from the transitions in very close bands. Nevertheless, at high energies, the sharp peaks may be accordance with inter-band optical transitions between valance and CBs that can be considerably far from each other.

The onset of absorption edge in $\text{Ba}_2\text{CePtO}_6$ is recorded at around 1.52 eV which is the same point from where the $\epsilon_2(\omega)$ rises from zero, in agreement with computed band gap energy. Near the threshold point, the absorption process comes from the dominant bands of the optical transition from Pt-5d orbital at VBM to the Ce-4f CB orbital. Afterwards, the $\alpha(\omega)$ rate increases with the photon energy toward the UV spectrum. This is due to the augmentation of the number of electrons that have an energy allowing them to interact with photons. Also, the titled compound demonstrates substantial optical absorption over a wide band of solar spectrum involving both VIS and UV bands with a strong wider peak noticed at about 5.2 eV. Thus, the compound under-study can be suggested as a potential material having possible applications in optoelectronics within VIS and UV regions. We note that in the VIS region, the absorption of $\text{Ba}_2\text{CePtO}_6$ is higher than that of $\text{Ba}_2\text{ZrCeO}_6$ reported by Kazim et al. (2022). As a result, $\text{Ba}_2\text{CePtO}_6$ is the most suitable contender for such uses because of its higher $\alpha(\omega)$ values. Since the elevated $\alpha(\omega)$ enhances the PV conversion efficiency, the observed high $\alpha(\omega)$ ($> 10^5 \text{ cm}^{-1}$) with a broad absorption band in the VIS range suggests that $\text{Ba}_2\text{CePtO}_6$ material is a potential candidate for PV absorber.

3.5.4 Optical conductivity

The conduction of electrons, with respect to particular incident photon, is controlled by $\sigma(\omega)$. In the present work, the $\sigma(\omega)$ has been conducted for $\text{Ba}_2\text{CePtO}_6$ compound material. Our results are depicted in Fig. 4e. However, at lower energies, the $\sigma(\omega)$ spectra show a zero-conductivity correlated with the zero absorption $\alpha(\omega)$. Likewise, the highest values of $\sigma(\omega)$ occur at nearly the same position of the maximum $\alpha(\omega)$. Additionally, we can clearly see that when the incident photon energy is less than E_g , $\sigma(\omega)$ is zero, meaning that the incident photons do not interact much with the electrons of $\text{Ba}_2\text{CePtO}_6$ within that photon energy range. Afterwards, a sudden increase to the first extreme peak of about $883 (\Omega \cdot \text{cm})^{-1}$ is observed in the VIS range at 2 eV. Furthermore, a multiple intense peaks of $\sigma(\omega)$ spectra indicate that $\text{Ba}_2\text{CePtO}_6$ is optically conductive in a wide range from VIS to UV and may have broad applications in this range. However, a maximum optical conductivity of $4658.24 (\Omega \cdot \text{cm})^{-1}$ noticed at 8.12 eV denotes that the material is more photon absorbent in the UV range.

3.5.5 Optical reflectivity

The reflectivity spectra against photon energy, $R(\omega)$, computed for the Ba₂CePtO₆ is exposed in Fig. 4c. The zero frequency limit $R(0)=R(\omega \rightarrow 0)$ is recorder as 15%. Then, the $R(\omega)$ increases with photon energy to extent a maximum value at UV region. The maximum reflectivity is found to occur when $\epsilon_1(\omega)$ goes below zero. Additionally, the most appreciable peaks values of the present $R(\omega)$ are noted in the energy ranging from 1.78 eV to afterwards. In the VIS spectrum, the material shows an insignificant maximum reflectivity of only 22% as its first reflectivity peak appear at around 1.78 eV indicating that the Ba₂CePtO₆ has a relatively high transparency in the VIS range and ensure the reliability of this material for optoelectronics devices applications.

3.5.6 Electron energy loss

The electron energy loss spectra $L(\omega)$ is also an indispensable optical parameter to be investigated. Usually this parameter is used to illustrate how fast electron travelling throughout a given homogeneous material loses energy in terms of scattering of light and heating of materials. Moreover, the interactions causing the loss of energy include mainly the intra-band and inter-band transitions together with both plasmon and phonon excitations. We note that, plasmons are collective oscillations of free electrons which cause sharp peaks in $L(\omega)$ spectrum. However, peaks in $L(\omega)$ diagram can also attributed to the inter-band transitions. Figure 4c shows $L(\omega)$ in the photon energy scope of 0–14 eV for the Ba₂CePtO₆ DPO. One can see that $L(\omega)$ spectra shows a set of peaks at different energy regions. Furthermore, the most appreciable peaks have been observed in the UV range. These peaks are derived from inter-band transitions whose widths are attributed to the phonon–phonon scattering. In the VIS range, the prominent peaks are located at around 2.28 eV. A nominal optical $L(\omega)$ in low energy side proves the usefulness of the present material for optoelectronics applications.

3.6 Thermoelectric transport properties

The current and promising applications of TE materials require the study of its heat-to-electricity conversion efficiency. Hence, understanding TE transport properties is of crucial importance in designing and improving the TE performances of materials. These can be evaluated by determining its TE parameters such as Seebeck coefficient (S), thermal conductivity (κ), electrical conductivity (σ), power factor ($PF=S^2\sigma$) and TE figure of merit ($ZT=\sigma S^2T/\kappa$) at varying temperatures. The interdependency of TE transport properties of a material can be pursued from a number of factors related to the electronic band profile near the E_F level. The key factor affecting the value of S is the occurrence of flat bands at the VBM which confirm the larger carrier's effective mass. While, the σ is crucially enhanced by the existence of a wider dispersive band at the VBM implying lighter effective mass and improved mobility. Furthermore, the observed flat and wider dispersive bands at the VBM, a moderate semiconducting E_g and adequate amount of TDOS at the vicinity of E_F confirm that the investigated compound is a promising candidate for TE applications. Consequently, these relevant results inspired us to explore its TE transport properties. As all these characteristics depend mainly on the carrier's concentration and thus, they cannot be controlled independently. However, to clearly see the doping contribution on these parameters, TE parameters are investigated against chemical potential in the range of -2

to 2 eV for three fixed temperatures, namely, 300 K, 600 K, and 900K. In this respect, we note that, the chemical potential describes the requisite quantity of energy for moving carriers against the faced Coulomb potential. Moreover, the positive value of chemical potential indicates n-type conductivity with an upward shift of the E_F level, whereas the negative values are associated with the p-type conductivity with a downward shift of E_F .

The chemical potential and the temperature based $\sigma(T, \mu)$, $S(T, \mu)$ and the electronic thermal conductivity $\kappa_e(T, \mu)$ are estimated by integrating the transport distribution function as follows (Ziman 2001; Allen 1996; Hurd 1972):

$$\sigma_{\alpha\beta}(T, \mu) = \frac{1}{V} \int \sigma_{\alpha\beta}(\varepsilon) \left[-\frac{\partial f(T, \varepsilon, \mu)}{\partial \varepsilon} \right] d\varepsilon \tag{8}$$

$$S_{\alpha\beta}(T, \mu) = \frac{1}{eTV\sigma_{\alpha\beta}(T, \mu)} \int \sigma_{\alpha\beta}(\varepsilon)(\varepsilon - \mu) \left[-\frac{\partial f(T, \varepsilon, \mu)}{\partial \varepsilon} \right] d\varepsilon \tag{9}$$

$$\kappa_{\alpha\beta}^e(T, \mu) = \frac{1}{e^2TV} \int \sigma_{\alpha\beta}(\varepsilon)(\varepsilon - \mu)^2 \left[-\frac{\partial f(T, \varepsilon, \mu)}{\partial \varepsilon} \right] d\varepsilon \tag{10}$$

where $\mu, \varepsilon, T, e, V, f, \alpha$ and β , correspond respectively to the chemical potential, the band energy, the absolute temperature, the electron charge, the volume of the primitive unit cell under investigation, the Fermi–Dirac function, and tensor independent indices. The coefficient of electrical conductivity $\sigma_{\alpha\beta}(\varepsilon)$ is reported as (Madsen and Singh 2006):

$$\sigma_{\alpha\beta}(\varepsilon) = \frac{1}{N} \sum_{i,k} \sigma_{\alpha\beta}(i, k) \times \frac{\delta(\varepsilon - \varepsilon_{i,k})}{\delta(\varepsilon)} = \frac{e^2}{N} \sum_{i,k} \tau_{i,k} v_{\alpha}(i, k) v_{\beta}(i, k) \times \frac{\delta(\varepsilon - \varepsilon_{i,k})}{\delta(\varepsilon)} \tag{11}$$

where $\tau_{i,k}$ and $v(i, k)$ refer respectively to the relaxation time and the group velocity.

Within the constant time relaxation (τ) approximation adopted here, S coefficient can be evaluated independently of any constraint. While, σ and κ_e is associated with the carrier relaxation time τ and therefore must be computed with respect to τ .

3.6.1 Seebeck coefficient

The S coefficient is a key measure of TE power of a material, or its ability to generate an electric potential due to the temperature difference across two contact materials. Moreover, a good TE material provides a large potential gradient induced by a small temperature variation between the two contacts. Furthermore, S can be referred to describe the carrier’s contribution in electronic transport. A positive magnitude of S exhibits p-type conduction due to the holes as dominant charge carriers; nevertheless $S < 0$ defines n-type conduction due to electrons. Figure 5a clearly shows the contribution of carriers to the S above ($\mu > \mu_F$) and below ($\mu < \mu_F$) the E_F level at three chosen temperatures, namely, 300, 600 and 900 K. It is clear that S shows a variation between -0.27 and 1.75 eV, while in the outside of this energy range, S has low and almost zero values. Moreover, the observed prominent peaks in the n-type side are consistent with the fact that in this energy range, the bands are less dispersive, which is a direct consequence of large effective mass, with the forbidden region in the vicinity of E_F , in that way fewer charge carriers are present. For the considered temperatures, the magnitude of peaks reduces remarkably as the temperature rises and the highest possible value of $|S|_{sup}$ has been noticed at 300 K. This behavior demonstrates

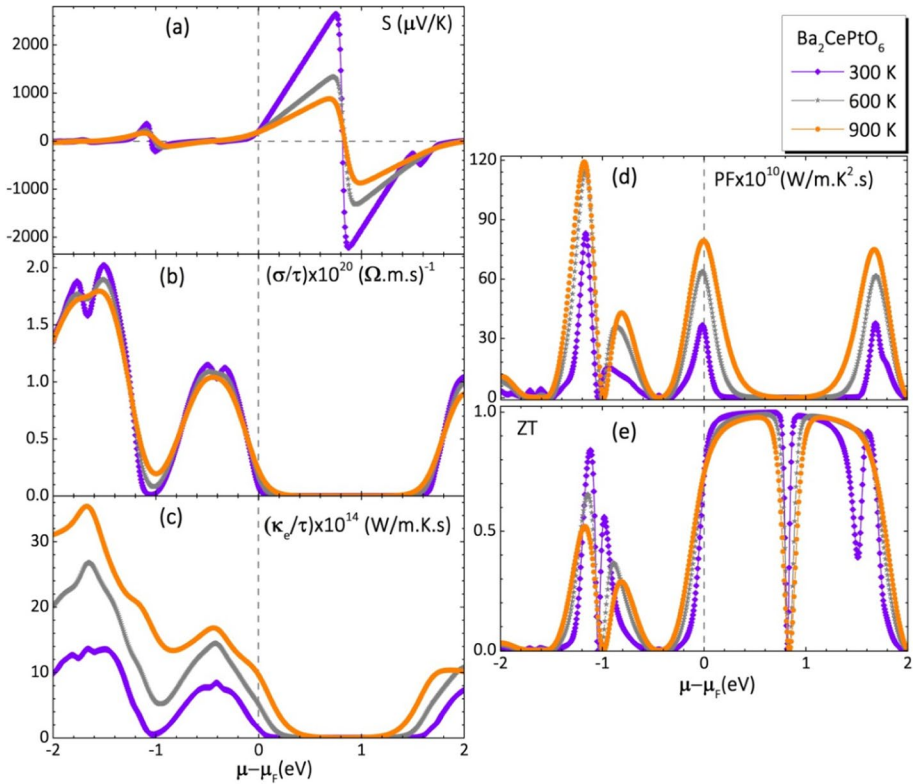


Fig. 5 Computed results of **a** seebeck coefficient (*S*) **b** electrical conductivity (σ/τ) **c** electronic thermal conductivity (κ_e/τ) **d** TE power factor (PF) and **e** TE figure of merit (ZT) of Ba₂CePtO₆ against $\mu-\mu_F$ for three selected temperatures

that the bound electrons are excited by acquiring a sufficient amount of thermal energy given rise to the electron–hole pairs. Moreover, the observed extreme values of the present *S* at different temperatures are listed in Table 5. As can be seen, the reported extreme values correspond to the narrow range of μ , thus they can be reached by a weak doping

Table 5 Highest values of TE properties for Ba₂CePtO₆ DOP at different temperatures for both p- and n-type doping case

Parameters	100 K		300 K		500 K		700 K		900 K	
	p-type	n-type	p-type	n-type	p-type	n-type	p-type	n-type	p-type	n-type
<i>S</i>] _{sup} (mV/K)	+0.86	−3.131	+0.36	+2.64	+0.25	+1.61	+0.20	+1.14	+0.19	+0.88
σ/τ (10 ²⁰ /Ω.m.s)	2.09	2.46	2.02	2.84	1.94	2.47	1.86	2.45	1.79	2.42
PF (10 ¹¹ W/K ² .m.s)	3.23	3.66	8.31	8.24	10.80	9.32	11.88	9.51	11.91	9.21
N (carrier/u.c.)	6.13	13.91	6.33	13.81	6.49	13.74	6.68	13.69	6.85	13.65
ZT	0.964	1.00	0.841	0.998	0.731	0.993	0.735	0.986	0.741	0.978

N represents the optimal concentration per primitive unit cell (carriers/u.c.) for highest PF

concentration which is useful in practice. While for higher μ , its value decreases gradually. In addition, from Table 5, we can notice that at the same temperature, the positive value of S is higher than the corresponding negative magnitude, signaling that $\text{Ba}_2\text{CePtO}_6$ compound reveals p-type conductivity.

3.6.2 Electrical conductivity

As seen in the Fig. 5b, for the selected temperatures, the increasing magnitude of μ for p- and n-type doped regions, σ/τ shows alternative peaks and valleys. Moreover, in the chemical potential range of 0.36–1.30 eV near the E_F level it appears to have no conductivity as there are no energy bands and this region is devoid of charge carriers. However, outside this range, the $\text{Ba}_2\text{CePtO}_6$ reveals a high σ/τ . Furthermore, the chemical potential dependence of σ/τ is similar at different temperatures. In contrast to the S coefficient, the peak values of σ/τ do not vary greatly with temperature. Consequently, the temperature has an insignificant effect on σ/τ in the investigated chemical potential window. Moreover, because the σ/τ is inversely correlated to the carrier's effective mass, the p-type doped region exhibits a relatively higher σ/τ than the n-type side owing to the observed light holes effective mass in the VB contrasted to electrons in the CB. Accordingly, the values of μ where σ/τ reaches its maximum value lie in a short range.

3.6.3 Electronic thermal conductivity

Another important parameter that influences the figure of merit is the thermal conductivity, κ , which needs to be reduced. This parameter corresponds to the rate of heat transferred through unit area of material under the temperature gradient of 1 K per meter. Instinctively, a good κ prevents a large temperature gradient from developing. It is well known that the flow in the compounds is mainly attributed to the carrier's motion and lattice vibrations (phonons). Therefore, the net κ is predominately composed of two main contributions: the electronic contribution, κ_e , caused by the carrier's motion, and the lattice contribution due to the lattice phonons κ_L which induces elastic waves that trigger the carriers ($\kappa = \kappa_e + \kappa_L$). Therefore, in the present contribution we have ignored the phonon component while the electronic is only accountable. For this reason, we have adopted the BoltzTrap ((Boltzmann Transport Properties) code based on semi-classical Boltzmann transport theory, which computes only the electronic part, to synthetically investigate the electronic transport properties. As seen in Fig. 5c, for p-type doping region we remark that at a particular temperature, with increasing μ , κ_e/τ increases quickly with temperature contrasted to σ/τ . Also, with tuning chemical potential the κ_e/τ increases substantially with temperature, ensuring that the κ_e/τ is mainly attributable to the free carriers. Furthermore, the p-type doped side exhibits higher κ_e/τ than the n-type side. Moreover, with the same trend as for electrical conductivity, we can clearly see that κ_e/τ is almost zero in a certain range of positive chemical potential with a negligible variation for varying temperatures which forecast that the studied perovskite has a highly potential for TE devices.

3.6.4 Thermoelectric power factor

The TE response efficiency of materials is evaluated without incorporation of κ_e/τ by the TE power factor ($\text{PF} = S^2\sigma/\tau$). Therefore, a remarkable S and σ/τ are essential in a possible TE material with a superior power factor, though their coexistence is unusual. It is clear

from Fig. 5d that, because of its high σ/τ , Ba₂CePtO₆ exhibits the highest PF in p-type doping region revealing that the electrons contribution in electronic transport is insignificant compared to the holes. Further, the observed pronounced peaks are directly connected to the doping level, indicating that the TE performance can be improved under appropriate doping levels. The predicted peak power factors values for p- and n-type regions are listed in Table 5. Both Fig. 5 and Table 5 demonstrate that in all circumstances, the PF shows the highest values at 900 K and it gradually decreases with temperature. The PF improvement with temperature is known to contribute positively to enhancing TE performances. Hence, the DPO under focus may find practicality in TE devices thanks to its higher PF values.

3.6.5 Figure of merit

The working efficiency of a TE material is specified in terms of the dimensionless quantity called the figure of merit ($ZT = \sigma S^2 T / \kappa$). Further, a material is considered to be a relevant TE material if its $ZT \geq 1$. On the basis of the above conferred electron transport properties, we have computed the figure of merit of Ba₂CePtO₆ DPO at different temperatures under p- and n-type doping levels. The obtained results are depicted in Fig. 5e. In n-type doping region, Fig. 5e indicates that the present compound exhibits a significant ZT over a wide range of chemical potential. Furthermore, ZT reaches its enhanced value of around unity noticed in the chemical potential windows where S becomes higher which is appreciable for TE applications. Similar to the PF, in the whole considered chemical potential range, all temperatures show similar trends. Moreover, owing to the enhancement of σ , two apparent peaks are present for the hole-doped material. Thus, ZT values exceed 0.841 and 0.998 at 300 K under an optimized p-type and n-type doping, respectively. Although, the relatively poor TE performance shown in p-type doping region, is mainly ascribed to the high thermal conductivity. Also, at the E_F level, the obtained ZT value is approximately equal to 0.741 which is found to be temperature independent. The highest values of $|ZT|_{\text{sup}}$ in both p- and n-type doping regions of the proposed material have been recorded in Table 5. Accordingly, these findings suggest that for Ba₂CePtO₆ DPO, the improvement of ZT is expected with a proper n-type doping. Consequently, Ba₂CePtO₆ emphasizes a great potential as a high-temperature TE material.

4 Conclusion

Double perovskite oxides are promising materials for optoelectronic and thermoelectric applications. In this paper, the structural, optoelectronic, and thermoelectric (TE) features of SC Ba₂CePtO₆ are explored systematically. The studied material is a stable cubic structure, stiffer, ductile with ionic bonding character and anisotropic. Also, the reported melting and Debye temperatures ensure its strong bonding and retention even for elevated temperatures. The broad band of solar spectrum, Ba₂CePtO₆ is found to be optically conductive with substantial optical absorption, low reflectivity, low energy loss and high refractive index. Furthermore, the TE properties show a significant value of figure of merit (ZT). Accordingly, the reported results ensure the reliability of Ba₂CePtO₆ for optoelectronics and thermoelectric applications even at higher temperatures. However, owing to the deficiency in theoretical and experimental data, these findings offer new pathway for TE and optoelectronic technologies and are expected to serve as a stimulated reference for the innovative investigations of Ba₂CePtO₆.

Acknowledgements The author (Tahani A. Alrebdi) extends her sincere appreciation to Princess Nourah bint Abdulrahman University Researchers Supporting Project number (PNURSP2024R71), Princess Nourah bint Abdulrahman University, Riyadh, Saudi Arabia. The authors extend their appreciation to the Deanship of Scientific Research at King Khalid University for funding this work through research groups program under grant number (RGP.2/583/44).

Author contributions Abderrazak Boutramane, Samah Al-Qaisi, Malak Azmat Ali, Tahani A. Alrebdi, wrote the main manuscript. Afaf Khadr Alqorashi, Ajay Singh Verma, Zeesham Abbas prepared figures. El Sayed Yousef, Ramesh Sharma, Muhammad Mushtaq reviewed the manuscript.

Funding No funding received.

Declarations

Conflict of interest The authors have no conflict of interest to declare that are relevant to the content of this article.

References

- Aczel, A.A., Clancy, J.P., Chen, Q., Zhou, H.D., Reig-i-Plessis, D., MacDougall, G.J., Ruff, J.P.C., Upton, M.H., Islam, Z., Williams, T.J., Calder, S., Yan, J.-Q.: Revisiting the Kitaev material candidacy of Ir^{4+} double perovskite iridates. *Phys. Rev. B* **99**, 134417–134428 (2019)
- Allen, P.B.: Boltzmann theory and resistivity of metals. In: Chelikowsky, J.R., Louie, S.G. (eds.) *Quantum Theory of Real Materials*, pp. 219–250. Kluwer, Boston (1996)
- Al-Qaisi, S., Rai, D.P., Alshahrani, T., Ahmed, R., Haq, B.U., Tahir, S.A., Khuili, M., Mahmood, Q.: Structural, elastic, thermodynamic, electronic, optical and thermoelectric properties of MgLu_2X_4 ($\text{X} = \text{S}, \text{Se}$) spinel compounds from ab-initio calculations. *Mater. Sci. Semicond.* **128**, 105766–105777 (2021)
- Al-Qaisi, S., Mushtaq, M., Alzahrani, J.S., Alkhalidi, H., Alrowaili, Z.A., Rached, H., Bakhtiar, U.H., Mahmood, Q., Al-Buriah, M.S., Morsi, M.: First-principles calculations to investigate electronic, structural, optical, and thermoelectric properties of semiconducting double perovskite Ba_2YBiO_6 . *Micro. Nano* **170**, 207397–207407 (2022a)
- Al-Qaisi, S., Malak, A.A., Tahani, A.A., Tuan, V.V., Morsi, M., Bakhtiar, U.H., Ahmed, R., Mahmood, Q., Afzal Tahir, S.: First-principles investigations of Ba_2NaO_6 double perovskite semiconductor: material for low-cost energy technologies. *Mater. Chem. Phys.* **275**, 125237–125247 (2022b)
- Al-Qaisi, S., Rached, H., Ali, M.A., Abbas, Z., Alrebdi, T.A., Hussein, K.I., Khuili, M., Rahman, N., Verma, A.S., Ezzeldien, M., Morsi, M.: A comprehensive first-principles study on the physical properties of $\text{Sr}_2\text{ScBiO}_6$ for low-cost energy technologies. *Opt. Quantum Electron.* **55**, 1015–1033 (2023)
- Amador, U., Hetherington, C.J.D., Moran, E., Alario-Franco, M.A.: $\text{Ba}_2\text{PrPtO}_6$: a novel double perovskite. *J. Solid State Chem.* **96**, 132–140 (1992)
- Anderson, M.T., Greenwood, K.B., Taylor, G.A., Poeppelmeier, K.R.: B-cation arrangements in double perovskites. *Prog. Solid State Chem.* **22**, 197–233 (1993)
- Bairwa, J.K., Rani, M., Kamlesh, P.K., Singh, R., Rani, U., Al-Qaisi, S., Kumar, T., Kumari, S., Verma, A.S.: Modeling and simulation of multifaceted properties of X_2NaO_6 ($\text{X} = \text{Ca}$ and Sr) double perovskite oxides for advanced technological applications. *J. Mol. Model.* **29**, 379–391 (2023)
- Behera, D., Al-Qaisi, S., Manzoor, M., Sharma, R., Srivastava, V., Al-Anazy, M., El Shiekh, E., Mukherjee, S.K.: First principles studies on optoelectronics and transport properties of KSrY ($\text{Y} = \text{Sb}, \text{Bi}$) for renewable energy application. *Mater. Sci. Eng. B* **297**, 116765–116776 (2023)
- Bharti, C., Sinha, T.P.: Dielectric properties of rare earth double perovskite oxide $\text{Sr}_2\text{CeSbO}_6$. *Solid State Sci.* **12**, 498–502 (2010)
- Bharti, C., Sinha, T.P.: Electrical analysis of a newly synthesized rare earth double perovskite oxide: $\text{Sr}_2\text{CeNbO}_6$. *Phys. b: Condens.* **406**, 624–627 (2011a)
- Bharti, C., Sinha, T.P.: Synthesis, structure and dielectric properties of a rare earth double perovskite oxide $\text{Ba}_2\text{CeTaO}_6$. *Mater. Res. Bull.* **46**, 1431–1436 (2011b)
- Bharti, C., Sinha, T.P.: Structural and ac electrical properties of a newly synthesized single phase rare earth double perovskite oxide: $\text{Ba}_2\text{CeNbO}_6$. *Phys. b: Condens.* **406**, 1827–1832 (2011c)
- Bildirici, M.E., Gökmenoğlu, S.M.: Environmental pollution, hydropower energy consumption and economic growth: evidence from G7 countries. *Renew. Sust. Energy Rev.* **75**, 68–85 (2017)

- Blaha, P., Schwarz, K., Madsen, G.K.H., Kvasnicka, D., Luitz, J.: WIEN2K: An Augmented Plane Wave and Local Orbitals Program for Calculating Crystal Properties. Vienna University of Technology, Austria (2001)
- Bobrov, V.B., Trigger, S.A., Van Heijst, G.J.F., Schram, P.P.J.M.: Kramers–Kronig relations for the dielectric function and the static conductivity of Coulomb systems. *EPL* **90**, 10003–10007 (2010)
- Bougherara, K., Al-Qaisi, S., Laref, A., Vu, T.V., Rai, D.P.: Ab initio insight of the electronic, structural, mechanical and optical properties of X₃P₂ (X= Mg, Ca) from GGA and hybrid functional (HSE06). *J. Supercond. Nov. Mag.* **35**, 79–86 (2022)
- Casapu, M., Grunwaldt, J.D., Maciejewski, M., Baiker, A., Eckhoff, S., Göbel, U., Wittrock, M.: The fate of platinum in Pt/Ba/CeO₂ and Pt/Ba/Al₂O₃ catalysts during thermal aging. *J. Catal.* **251**, 28–38 (2007)
- Chen, L., Yuan, C., Xue, J., Wang, J.: B-site ordering and magnetic behaviours in Ni doped perovskite Sr₂FeMoO₆. *J. Phys. D Appl. Phys.* **38**, 4003–4008 (2005)
- Chen, P., Podraza, N.J., Xu, X.S., Melville, A., Vlahos, E., Gopalan, V., Ramesh, R., Schlom, D.G., Musfeldt, J.L.: Optical properties of quasi-tetragonal BiFeO₃ thin films. *Appl. Phys. Lett.* **96**, 131907–131909 (2010)
- Dar, S.A., Sharma, R., Srivastava, V., Sakalle, U.K.: Investigation on the electronic structure, optical, elastic, mechanical, thermodynamic and thermoelectric properties of wide band gap semiconductor double perovskite Ba₂InTaO₆. *RSC Adv.* **9**, 9522–9532 (2019)
- Das, H., De Raychaudhury, M., Saha-Dasgupta, T.J.A.P.L.: Moderate to large magneto-optical signals in high T_c double perovskites. *Appl. Phys. Lett.* **92**, 201912–201914 (2008)
- Dutta, A., Mukhopadhyay, P.K., Sinha, T.P., Dipankar, D., Shannigrahi, S.: Structural and magnetic properties of double perovskite oxide Ba₂CeSbO₆. *Solid State Sci.* **58**, 64–69 (2016)
- Faizan, M., Murtaza, G., Khan, S.H., Khan, A., Mehmood, A., Khenata, R., Hussain, S.: First-principles study of the double perovskites Sr₂XO₆ (X= Li, Na, Ca) for spintronics applications. *Bull. Mater. Sci.* **39**, 1419–1425 (2016)
- Fu, W.T., Ijdo, D.J.W.: X-ray and neutron powder diffraction study of the double perovskites Ba₂LnSbO₆ (Ln= La, Pr, Nd and Sm). *J. Solid State Chem.* **178**, 2363–2367 (2005)
- Gajdoš, M., Hummer, K., Kresse, G., Furthmüller, J., Bechstedt, F.: Linear optical properties in the projector-augmented wave methodology. *Phys. Rev. B* **73**, 045112–045120 (2006)
- Hatakeyama, T., Takeda, S., Ishikawa, F., Ohmura, A., Nakayama, A., Yamada, Y., Matsushita, A., Yea, J.: Photocatalytic activities of Ba₂RbBiO₆ (R = La, Ce, Nd, Sm, Eu, Gd, Dy) under visible light irradiation. *J. Ceram. Soc. Jpn.* **118**, 91–95 (2010)
- Hilal, M., Rashid, B., Khan, S.H., Khan, A.: Investigation of electro-optical properties of InSb under the influence of spin-orbit interaction at room temperature. *Mater. Chem. Phys.* **184**, 41–48 (2016)
- Hill, R.: The elastic behaviour of a crystalline aggregate. *Proc. Phys. Soc. A* **65**, 349–354 (1952)
- Himanshu, A.K., Kumar, S., Dey, U., Ray, R.: Multiple low-energy excitons and optical response of d0 double perovskite Ba₂ScTaO₆. *Phys. b: Condens.* **637**, 413856–413863 (2022)
- Hurd, C.M.: *The Hall Effect in Metals and Alloys*. Plenum Press, New York-London (1972)
- Ivanovski, K., Hailemariam, A., Smyth, R.: The effect of renewable and non-renewable energy consumption on economic growth: non-parametric evidence. *J. Clean. Prod.* **286**, 124956–124970 (2021)
- Jasiukiewicz, C., Karpus, V.: Debye temperature of cubic crystals. *Solid State Commun.* **128**, 167–169 (2003)
- Kato, H., Okuda, T., Okimoto, Y., Tomioka, Y., Takenoya, Y., Ohkubo, A., Kawasaki, M., Tokura, Y.: Metallic ordered double-perovskite Sr₂CrReO₆ with maximal Curie temperature of 635 K. *Appl. Phys. Lett.* **81**, 328–330 (2002)
- Kazim, M.Z., Yassen, M., Shatha, A.A., Mudassir, I., Mubashar, N., Zahid, M., Neffati, R.: DFT study of optoelectronic and thermoelectric properties of cubic Ba₂ZrMO₆ (M=Ce, Ti) double perovskites. *J. Solid State Chem.* **315**, 123419–123427 (2022)
- Kockelmann, W., Adroja, D.T., Hillier, A.D., Wakeshima, M., Izumiyama, Y., Hinatsu, Y., Knight, K.S., Visser, D., Rainford, B.D.: Neutron diffraction and inelastic neutron scattering investigations of the ordered double perovskite Ba₂PrIrO₆. *Phys. b: Condens.* **378**, 543–545 (2006)
- Korchagina, S.K., Shevchuk, Y.A.: Low-frequency and microwave dielectric properties of Ba₂LnTaO₆ (Ln= La, Pr, Sm, Dy, Ce, Gd, Nd, Tm, Tb) ceramics. *Inorg. Mater.* **42**, 64–67 (2006)
- Li, X.Q., Zhao, J.J., Xu, J.C.: Mechanical properties of bcc Fe–Cr alloys by first-principles simulations. *Front. Phys.* **7**, 360–365 (2012)
- Lufaso, M.W., Barnes, P.W., Woodward, P.M.: Structure prediction of ordered and disordered multiple octahedral cation perovskites using SPuDS. *Acta Crystallogr. b: Struct. Sci. Cryst. Eng. Mater.* **62**, 397–410 (2006)
- Madsen, G.K., Singh, D.J.: BoltzTraP. A code for calculating band-structure dependent quantities. *Comput. Phys. Commun.* **175**, 67–71 (2006)

- Madsen, G.K., Blaha, P., Schwarz, K., Sjöstedt, E., Nordström, L.: Efficient linearization of the augmented plane-wave method. *Phys. Rev. B* **64**, 195134–195142 (2001)
- Mantziaris, S., Iliopoulos, C., Theodorakopoulou, I., Petropoulou, E.: Perennial energy crops vs. durum wheat in low input lands: economic analysis of a Greek case study. *Renew. Sust. Energy Rev.* **80**, 789–800 (2017)
- Mebed, A., Mushtaq, M., Muhammad, I., Lone, I.U.N., Samah, A.Q., Algethami, N., EL-Shamy, E.F., Laref, A., AL-Hosiny, N.M.: Structure, half-metallic and magnetic properties of bulk and (001) surface of Rb_2XMoO_6 ($X = Cr, Sc$) double perovskites: a DFT + U study. *Phys. Scr.* **98**, 015807–015820 (2023)
- Mostafaiepour, A., Bidokhti, A., Fakhrazad, M.B., Sadegheih, A., Mehrjerdi, Y.Z.: A new model for the use of renewable electricity to reduce carbon dioxide emissions. *Energy* **238**, 121602 (2022)
- Murnaghan, F.D.: The compressibility of media under extreme pressures. *Proc. Natl. Acad. Sci. u.s.a.* **30**, 244–247 (1944)
- Ouchetto, K., Archambault, F., Pineau, A., Choynet, J.: Chemical and structural characterization of a new barium ceroplatinate: Ba_2CePtO_6 a double perovskite mixed oxide. *J. Mater. Sci.* **10**, 1277–1279 (1991)
- Penn, D.R.: Wave-number-dependent dielectric function of semiconductors. *Phys. Rev.* **128**, 2093–2097 (1962)
- Perdew, J.P., Burke, K., Ernzerhof, M.: Generalized gradient approximation made simple. *Phys. Rev. Lett.* **77**, 3865–3868 (1996)
- Pettifor, D.: Theoretical predictions of structure and related properties of intermetallics. *Mater. Sci. Technol.* **8**, 345–349 (1992)
- Pugh, S.: XCH. Relations between the elastic moduli and the plastic properties of polycrystalline pure metals. *Lond. Edinb. Dublin Philos. Mag. J. Sci.* **45**, 823–843 (1954)
- Rammeh, N.: Crystal structure, electronic and magnetic properties of double perovskite Ba_2FeWO_6 : a combined experimental–theoretical study. *Phys. b: Condens.* **481**, 217–223 (2016)
- Rani, U., Kamlesh, P.K., Joshi, T.K., Sharma, S., Gupta, R., Al-Qaisi, S., Verma, A.S.: Alkaline earth based antiperovskite $AsPX_3$ ($X = Mg, Ca, \text{ and } Sr$) materials for energy conversion efficient and thermoelectric applications. *Phys. Scr.* **98**, 075902–075920 (2023)
- Ray, R., Himanshu, A.K., Sen, P., Kumar, U., Richter, M., Sinha, T.P.: Effects of octahedral tilting on the electronic structure and optical properties of d0 double perovskites A_2ScSbO_6 ($A = Sr, Ca$). *J. Alloys Compd.* **705**, 497–506 (2017)
- Reddy, Y., Suresh, Y., Markandeya, B., Appa, R., Bhikshamaiah, G.: Characterization and impedance study of Ba_2CeZrO_6 double perovskite. *J. Mater. Sci. Mater. Electron.* **29**, 2966–2973 (2018)
- Retuerto, M., Alonso, J.A., Martínez-Lope, M.J., Martínez, J.L., García-Hernández, M.: Record saturation magnetization, Curie temperature, and magnetoresistance in Sr_2FeMoO_6 double perovskite synthesized by wet-chemistry techniques. *Appl. Phys. Lett.* **85**, 266–268 (2004)
- Retuerto, M., Alonso, J.A., García-Hernández, M., Martínez-Lope, M.J.: Synthesis, structure and magnetic properties of the new double perovskite Ca_2CrSbO_6 . *Solid State Commun.* **139**, 19–22 (2006)
- Saha-Dasgupta, T.: Double perovskites with 3d and 4d/5d transition metals: compounds with promises. *Mater. Res. Express.* **7**, 014003–014015 (2020)
- Schreiber, E., Anderson, O.L., Soga, N., Bell, J.F.: Elastic constants and their measurement. *J. Appl. Mech.* **42**, 747–748 (1975)
- Schwarz, K., Blaha, P., Madsen, G.K.: Electronic structure calculations of solids using the WIEN2k package for material sciences. *Comput. Phys. Commun.* **147**, 71–76 (2002)
- Slavney, A.H., Hu, T., Lindenberg, A.M., Karunadasa, H.I.: A bismuth-halide double perovskite with long carrier recombination lifetime for photovoltaic applications. *J. Am. Chem. Soc.* **138**, 2138–2141 (2016)
- Snaith, H.J.: Perovskites: the emergence of a new era for low-cost, high-efficiency solar cells. *J. Phys. Chem. Lett.* **4**, 3623–3630 (2013)
- Soukiasian, A., Tian, W., Vaithyanathan, V., Haeni, J.H., Chen, L.Q., Xi, X.X., Schlom, D.G., Tenne, D.A., Sun, H.P., Pan, X.Q., Choi, K.J.: Growth of nanoscale $BaTiO_3/SrTiO_3$ superlattices by molecular-beam epitaxy. *J. Mater. Res.* **23**, 1417–1432 (2008)
- Tarbi, A., Chtouki, T., Bouich, A., Elkouari, Y., Erguig, H., Migalska-Zalas, A., Aissat, A.: InP/InGaAsP thin films based solar cells: lattice mismatch impact on efficiency. *Opt. Mater.* **131**, 12704–12711 (2022)
- Tarbi, A., Chtouki, T., Sellam, M.A., Elkouari, Y., Erguig, H., Migalska-Zalas, A.: Predicting the band-gap energy of distorted $GaSb_xAs_{1-x}$ and $InSb_xAs_{1-x}$ using design of experiment (DoE) and artificial intelligence (AI): a comparative study. *J. Phys. Chem. Solids* **175**, 111180–111186 (2023a)

- Tarbi, A., Chtouki, T., Erguig, H., Migalska-Zalas, A., Aissat, A.: Modeling and optimization of Sb and N resonance states effect on the band structure of mismatched III-NV alloys using artificial neural networks. *Mater. Sci. Eng. B* **290**, 116312–116321 (2023b)
- Tarbi, A., Chtouki, T., Sellam, M.A., Benahmed, A., El Kouari, Y., Erguig, H., Migalska-Zalas, A., Goncharova, I., Taboukhat, S.: Optimization of ultra-thin CIGS-based solar cells by strained In_{1-x}Ga_xAs absorption layer: ID SCAPS modeling. *J. Comput. Electron.* **22**, 1–8 (2023c)
- Tariq, M., Ali, M.A., Laref, A., Murtaza, G.: Anion replacement effect on the physical properties of metal halide double perovskites Cs₂AgInX₆ (X= F, Cl, Br, I). *Solid State Commun.* **314**, 113929–113936 (2020)
- Tran, F., Blaha, P.: Accurate band gaps of semiconductors and insulators with a semilocal exchange-correlation potential. *Phys. Rev. Lett.* **102**, 226401–226405 (2009)
- Vasala, S., Karppinen, M.: A2B'B''O6 perovskites: a review. *Prog. Solid State Chem.* **43**, 1–36 (2015)
- Wang, J., Yip, S., Phillpot, S.R., Wolf, D.: Crystal instabilities at finite strain. *Phys. Rev. Lett.* **71**, 4182–4185 (1993)
- Wu, M., Fang, L., Liu, L., Li, G., Elouadi, B.: Dielectric and ferroelectric properties of (1-x) BiFeO_{3-x}Bi_{0.5}Na_{0.5}TiO₃ solid solution. *Ferroelectrics* **478**, 18–25 (2015)
- Yin, W.J., Weng, B., Ge, J., Sun, Q., Li, Z., Yan, Y.: Oxide perovskites, double perovskites and derivatives for electrocatalysis, photocatalysis, and photovoltaics. *Energy Environ. Sci.* **12**, 442–462 (2019)
- Ziman, J.M.: *Electrons and Phonons: The Theory of Transport Phenomena in Solids*. Oxford University Press, London (2001)

Publisher's Note Springer Nature remains neutral with regard to jurisdictional claims in published maps and institutional affiliations.

Springer Nature or its licensor (e.g. a society or other partner) holds exclusive rights to this article under a publishing agreement with the author(s) or other rightsholder(s); author self-archiving of the accepted manuscript version of this article is solely governed by the terms of such publishing agreement and applicable law.

Authors and Affiliations

Abderrazak Boutramine¹ · Samah Al-Qaisi² · Malak Azmat Ali³ · Tahani A. Alrebdi⁴ · Afaf Khadr Alqorashi⁵ · Ajay Singh Verma⁶ · Zeesham Abbas⁷ · El Sayed Yousef^{8,9} · Ramesh Sharma¹⁰ · Muhammad Mushtaq¹¹

✉ Abderrazak Boutramine
Abderrazak.boutramine@gmail.com

✉ Samah Al-Qaisi
samah.qaisi@gmail.com

Malak Azmat Ali
azmatupesh@gmail.com

Tahani A. Alrebdi
taalrebdi@pnu.edu.sa

Afaf Khadr Alqorashi
a.alkorshy@tu.edu.sa

Ajay Singh Verma
drjayphy@gmail.com

Zeesham Abbas
zeeshamabbas035@gmail.com

El Sayed Yousef
omn-yousaf2000@yahoo.com

Ramesh Sharma
sharmadft@gmail.com

Muhammad Mushtaq
mushtaq325@gmail.com

- ¹ Ibn Zohr University, Agadir 80000, Morocco
- ² Palestinian Ministry of Education and Higher Education, Nablus, Palestine
- ³ Department of Physics, Government Post Graduate Jahanzeb College Saidu Sharif, Swat 19130, Khyber Pakhtunkhwa, Pakistan
- ⁴ Department of Physics, College of Science, Princess Nourah Bint Abdulrahman University, Riyadh, Saudi Arabia
- ⁵ Department of Physics, Faculty of Science, Taif University, Taif 21944, P.O. Box 11099, Saudi Arabia
- ⁶ Division of Research and Innovation, School of Applied and Life Sciences, Uttaranchal University, Dehradun 248007, India
- ⁷ Department of Nanotechnology and Advanced Materials Engineering, Sejong University, Seoul, Republic of Korea
- ⁸ Research Center for Advanced Materials Science (RCAMS), King Khalid University, Abha 61413, P. O. Box 9004, Saudi Arabia
- ⁹ Physics Department, Faculty of Science, King Khalid University, Abha, P. O. Box 9004, Saudi Arabia
- ¹⁰ Department of Applied Science, Feroze Gandhi Institute of Engineering and Technology, Raebareli 229001, India
- ¹¹ Department of Physics, University of the Poonch, Rawalakot 12350, Pakistan